TURBULENT DRAG REDUCTION/ENHANCEMENT IN A 304 STAINLESS STEEL RECTANGULAR CHANNEL FUNCTIONALIZED WITH A FEMTOSECOND LASER

Henry Ems*, Aaron Ediger, Alfred Tsubaki, Craig Zuhlke, Dennis Alexander, George Gogos

University of Nebraska-Lincoln, Lincoln, NE 68508, USA

ABSTRACT

In this paper, we present methods for enhancing or reducing drag experienced by metallic surfaces (304 stainless steel) functionalized with a femtosecond laser. Experiments were conducted with purified water (0.2 μm filtration). Femtosecond laser surface processing (FLSP) was performed on 304 stainless steel plates to create angled microstructures, which mimic those of shark skin. Data were collected at different Reynolds numbers by varying the mass flow rate. Data were recorded after steady state was reached. The processed plates were superhydrophilic and were used to obtain the friction factor in a rectangular channel test section over Reynolds numbers ranging from 8,000 to 13,000. For a superhydrophilic rectangular channel with angled structures, drag enhancement was measured with respect to smooth (unprocessed) surfaces over the total range of Reynolds numbers tested. After superhydrophilic testing was completed, the surfaces were coated with fluorinated silane using evaporative deposition that made the plates hydrophobic. The hydrophobic plates were then tested in the rectangular channel setup to obtain the friction factor. With the addition of an acrylic viewport, the presence of an air layer (plastron) was observed that sheds light to the friction factor data obtained for hydrophobic plates. Drag reduction was shown for Reynolds numbers that were accompanied with a thin plastron. When the plastron fully degraded, the surface was fully wetted, and the friction factor value shifted towards just below the superhydrophilic value.

NOMENCLATURE

θ_i	contact angle of a surface	(°)	d_h	hydraulic diameter	(m)
f_i	fraction of surface in contact	(1)	U	mean velocity	(m/s)

INTRODUCTION

Surface drag modification is of great interest for both civilian and military applications. Frictional drag is important in hydrodynamic situations as 50% of drag on ships and 60% of drag on submarines is due to skin friction [1]. The shipping industry has also had a tremendous impact to fuel usage and CO_2 emissions [2,3]. By creating a slip flow boundary condition, where there is a fluid velocity at the stationary wall, the shear stress at the interface between the fluid and the surface is decreased. Maintaining a slip flow boundary condition, the necessary pumping power to achieve the desired flow rate can be dramatically reduced or the speed of a boat increased during sailing. In 1823, Claude-Louis Navier introduced the idea of a slip condition at the boundary wall [4]. There are two fundamental characteristics for slip flow: the slip velocity and the slip length. The slip velocity is the velocity of the fluid at the wall, while the slip length is the imaginary distance below the surface where there would be zero velocity. Figure 1 shows a schematic for the slip flow boundary condition in a Couette parallel plate flow configuration. The slip length is largest for fluid flow when a uniform gas layer is present between the liquid and solid interface, however, is not stable

*Henry Ems: henryems@huskers.unl.edu

without external assistance. The use of non-wetting microstructures to create pockets of gas between the liquid and solid interface has been proven to be effective for reducing drag and more stable with respect to time [5].

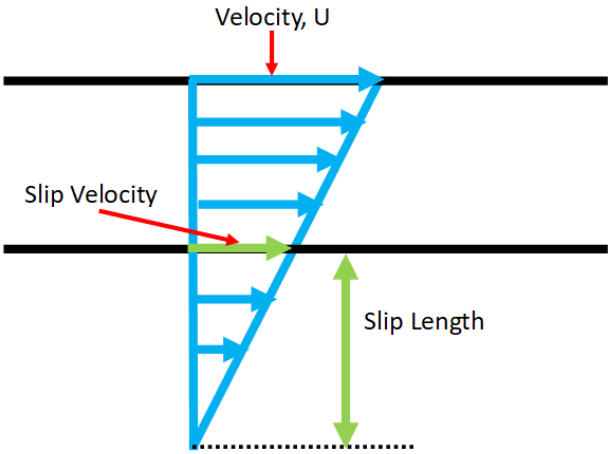

Figure 1. Slip flow for Couette flow in parallel plates.

Research has been performed to decrease the shear stress at the fluid-wall interface in various configurations including flows in a pipe [6–8], channel [9–16], microchannel [17–28], concentric cylinders [29–31], external flow [10,32,41–44,33–40], and flows past free-falling bodies [45]. Methods that have been investigated to reduce frictional drag include superhydrophobic surfaces[6–12,14–23,26–31,34–39,44,46,47], geometry modification [12,13,45,46], polymer additives [32,33,40–42,48–55], bubble/gas injection [32,40,41,43], lubricated surfaces [56], and vapor layer wettability of a heated surface [29]. Drag reduction from water repellant/superhydrophobic surfaces is directly related to the wettability of the surface. The wettability of the surface is influenced by the surface chemistry and the surface microstructures/nanostructures [57,58].

Past decades have seen an increase in attention towards the wettability of surfaces, specifically water repellant/superhydrophobic surfaces. The wettability of a surface is defined by the contact angle between the surface and a sessile water droplet. The contact angle, θ_E, of a homogeneous surface is defined by the Young's relation which considers the surface tension at each interface between the solid, liquid, and vapor. The Young's relation equation is shown in Equation 1, the surface tension of the solid-vapor, solid-liquid, and liquid-vapor interfaces are given by σ_{SV}, σ_{SL}, and σ_{LV} respectively[58–60].

$$cos\theta_E = \frac{\sigma_{SV} - \sigma_{SL}}{\sigma_{LV}} \quad (1)$$

If $\theta_E < 90°$ the surface is described as hydrophilic, however, if $\theta_E > 90°$ the surface is defined as hydrophobic or water repellant. In extreme cases, surfaces with a contact angle near 0° are defined as superhydrophilic or wicking, while surfaces with contact angles larger than 150° and low roll-off angles are defined as superhydrophobic [60].

To create a superhydrophobic surface, a Cassie-Baxter wetting state is desired. In a Cassie-Baxter wetting state, shown in Figure 2, the water does not wet the entire surface but instead sits on top of entrapped air [58,60]. The contact angle, θ, for a surface in the Cassie-Baxter wetting state can be found using Equation 2 where the fraction of the droplet in contact with the surface is f_1, the contact angle of surface 1 is given by θ_1, and the fraction of the droplet in contact with air is f_2.

$$cos\theta = f_1 cos\theta_1 - f_2 \quad (2)$$

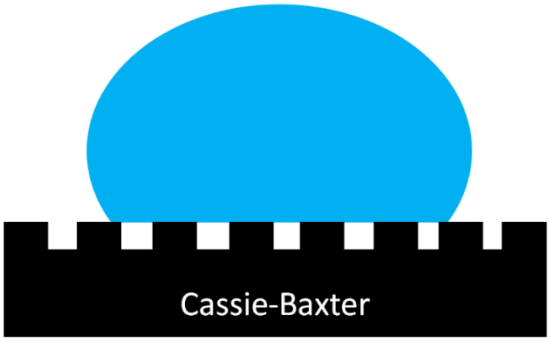

Figure 2. Cassie-Baxter wetting state.

Superhydrophobic surfaces are sought after in drag research for their ability to form an air layer, plastron, when submerged in water. With the presence of plastron, shown in Figure 3, an "air-bearing" is created during fluid flow resulting in a slip velocity and slip length, and therefore decreasing the shear strass at the interface of the water. The slip length is largest for fluid flow when a uniform gas layer is present between the liquid and solid interface, however, this condition is not stable without external assistance. The use of superhydrophobic multiscale surfaces to create pockets of gas between the liquid and solid interface has proven to be an effective method for reducing drag and is more stable with respect to time. After the plastron has been depleted, and the superhydrophobic surface is completely wetted, the slip length is still present though decreased significantly [5].

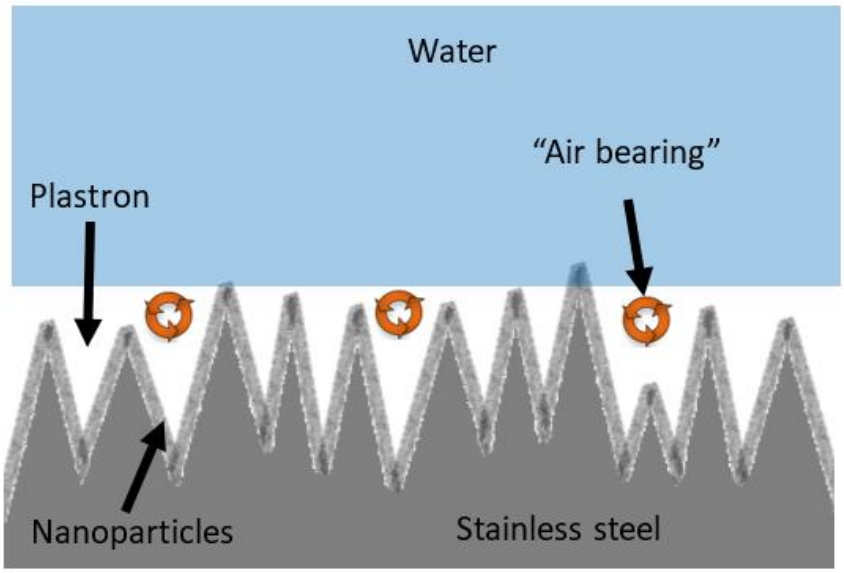

Figure 3. Drag reduction schematic for superhydrophobic surface.

In this paper, functionalized superhydrophilic and hydrophobic surfaces using femtosecond laser surface processing and silane deposition are discussed. Drag reduction results are presented for turbulent flow over the functionalized surfaces in a rectangular channel configuration. Various techniques for analyzing the drag results are also discussed.

FEMTOSECOND LASER SURFACE PROCESSING

Femtosecond laser surface processing (FLSP) is rapidly emerging as a powerful method for the fabrication of multiscale surface structures (surfaces with roughness on both the micrometer and nanometer scales). Multiscale surfaces are considered to be biologically inspired because of their occurrence in nature; an example of a multiscale surface is the superhydrophobic lotus leaf, which exhibits self-cleaning due to the nature of its multiscale surface structures [61,62]. Multiscale surface structures have been shown to strongly affect the wettability of a surface, which can result in either the enhancement or the reduction of surface drag.

The size and shape of the self-organized surface structures fabricated via FLSP are controlled through various fabrication parameters including laser fluence, the number of laser shots per area, and the processing environment. The generation of surface features is achieved through illumination of the sample using laser fluence values above the material's ablation threshold. Examples of scanning electron microscope (SEM) images of FLSP structures can be seen in Figure 4.

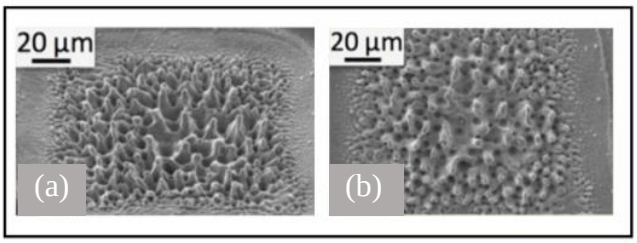

Figure 4. Scanning electron microscope images of structures on 304 stainless steel. The (a) image was taken at a viewing angle of 45° to show the structure height relative to the original surface; the (b) image was taken at normal incidence to show the size and separation of the structures.

FLSP FABRICATION SPECIFICATIONS

Femtosecond laser processed surfaces consisting of angled microstructures were used for this study. The laser used to produce the functionalized samples was a Coherent Astrella, Ti:Sapphire femtosecond laser system (Figure 5), which was capable of producing 6 mJ, 35 fs pulses at a 1 kHz repetition rate with a center wavelength of 800 nm . The pulse length and chirp were monitored using an autocorrelator measurement. The position of the sample with respect to the laser focal volume is controlled using computer guided Zaber Technologies translation stages with three axes of motion. The laser power is controlled using a half-waveplate and a polarizer combination. A lens with a six-inch focal length, is used to focus the femtosecond pulses, which have a Gaussian spatial profile. It should be noted that in a previous study on a sample processed in a similar manner, no foreign materials (materials not native to the substrate) were detected in the nanoparticle layer [63].

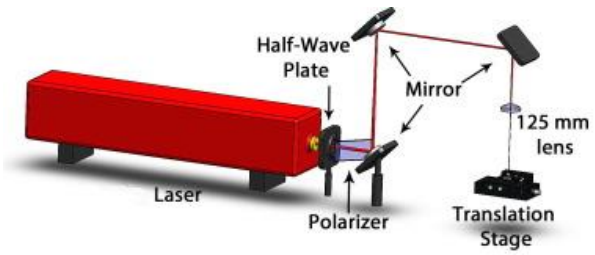

Figure 5. Femtosecond laser surface processing setup.

The impact of multiscale surface structures produced via FLSP on the drag on a surface of 304 stainless steel (SS304) was investigated through the characterization of one FLSP sample with a

smooth sample as a control. Characterization of the smooth and laser processed SS304 surfaces was carried out using 3D profilometry scans, which were taken with a 3D confocal laser scanning microscope (Keyence VK-X200). The laser parameters used to functionalize the surface were a peak fluence of 3.25 J/cm^2 and a pulse count of 5755. As can be seen from Figure 6a and Figure 6b, the FLSP surface consists of self-assembled angled microstructures, which closely mimic those seen on shark skin. Figure 6c shows the incident angle for fabricating the angled microstructures via FLSP. The microstructure orientation with respect to the flow direction is given in Figure 6d. The direction of the flow was in the same direction as the microstructures, simulating flow past a shark's skin.

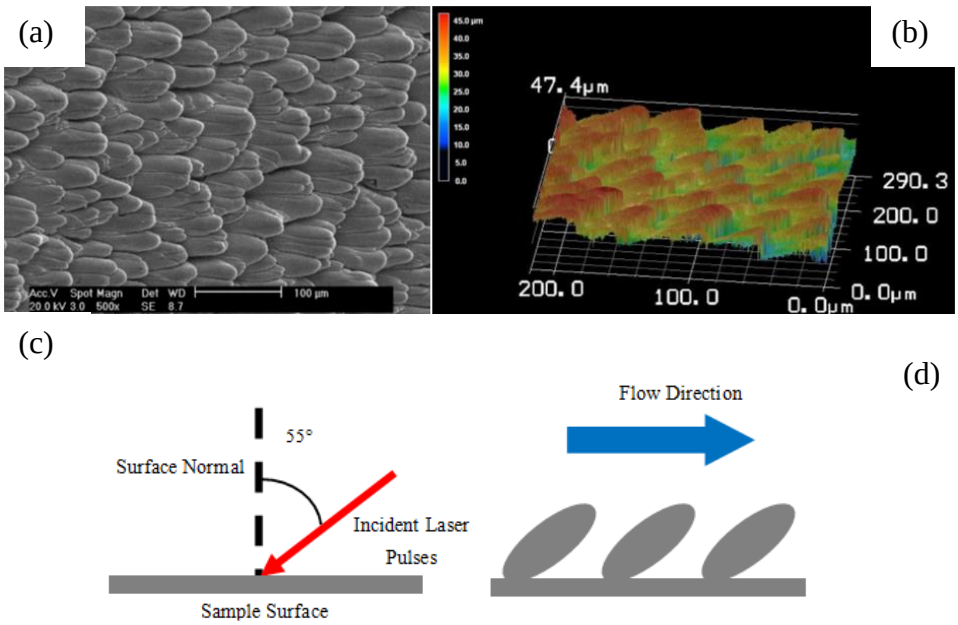

Figure 6. (a) SEM image of FLSP stainless steel sample. (b) LSCM image of FLSP 304 stainless steel sample. (c) Diagram showing the laser's incident angle during processing to produce the shark-skin-like angled structures. (d) Diagram for the direction of the microstructures.

From the 3D confocal laser scanning microscope data, microstructure height and peak protrusion information could be obtained: microstructures on the FLSP surface had an average peak-to-valley height of 36 µm and the peaks were 17 µm below the surface. These measurements were taken at various random locations on each surface. It should be noted that the sample was kept superhydrophilic (contact angle of zero degrees) through storage in purified water (0.2 µm filtration). If the contact angle ever went above zero degrees, the sample was heated at 200°C to release any absorbed hydrocarbons from the surface. Hydrocarbons are present in air and, upon absorption on the surface, affect the wettability of FLSP samples [64]. Table 1 gives a summary of results from the surface characterization.

Table 1. Measured Surface Characteristics

Sample	Peak-to-Valley Height (µm)	Peak height below the original surface (µm)
Angled Microstructures	36	17

The hydrophobic surface was formed by evaporative deposition of a silane onto the FLSP surface. The silane used was perfluorooctyltriethoxysilane and was evaporated at 200 degrees Celsius for 3 hours. Laser scanning confocal microscope measurements, performed at the University of Nebraska-Lincoln, confirmed the presence of a plastron when a superhydrophobic femtosecond laser surface processed (FLSP) sample was submerged under water [65]. The plastron was located near the top of the peaks, as shown in Figure 7, with only a few peaks protruding through.

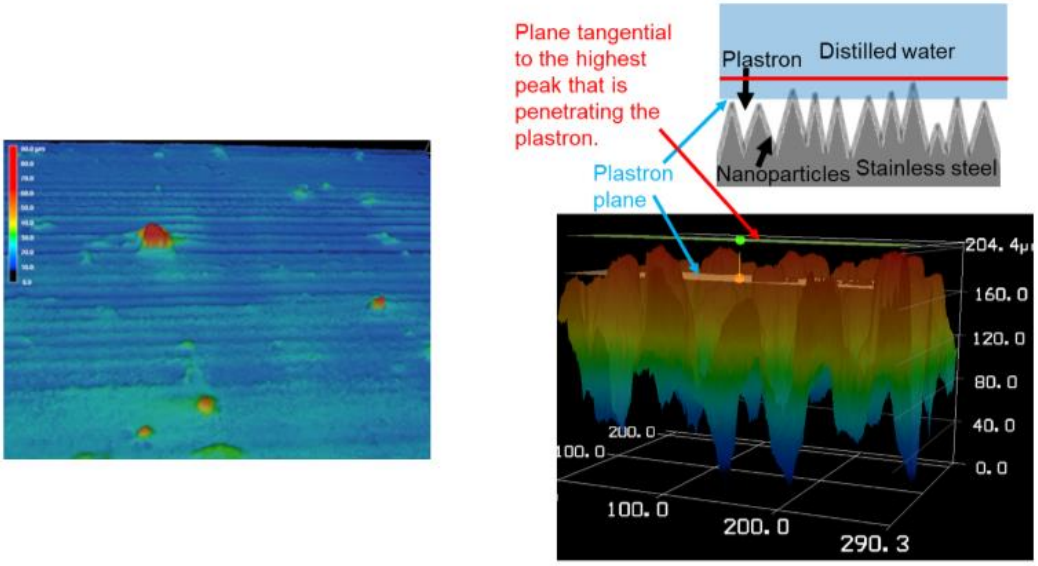

Figure 7. Laser scanning confocal image of the plastron height

EXPERIMENTAL SET UP

A flow loop, shown in Figure 8, was designed to measure the pressure drop and flow rate over a rectangular cross section with varying microstructures/coatings on the surfaces of the channel. A Grundfos CRE 3-11 pump was used to pump purified water (0.2 μm filtration) through the loop. The volumetric flowrate through the test section was measured with a TRG standard turbine flow meter. A differential pressure transducer (PX409-10WDWU5V) was used to measure the pressure drop over the channel test section. A K-type thermocouple was placed at the exit of the test section to monitor the temperature of the fluid over time. After exiting the test section, the water returned to the reservoir. The data acquisition system used was a National Instruments NI USB-6210. Temperature, flowrate, and pressure drop measurements were collected through an integrated LabVIEW program.

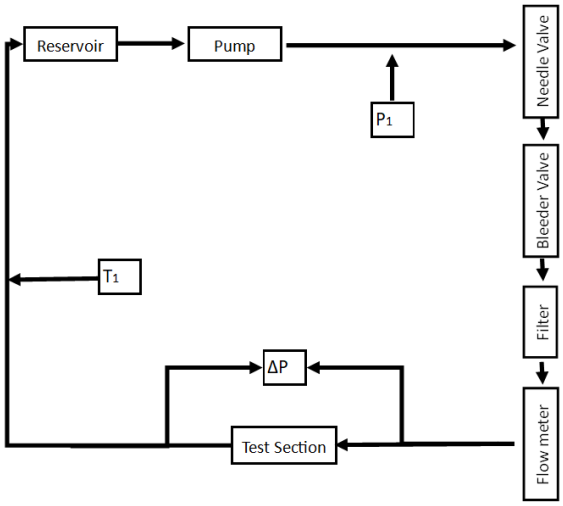

Figure 8. Flow loop design.

An assembled and cross section view of the test section is shown in Figure 9. Multiple 304 stainless steel plates are used to form the rectangular test section. The channel test section is 4 cm wide, 5 mm tall, and 45 cm long from pressure port to pressure port. Laser processing and a surface coating were used on the 304 stainless steel plates to test drag enhancement/reduction across the surface for superhydrophilic and hydrophobic angled microstructures.

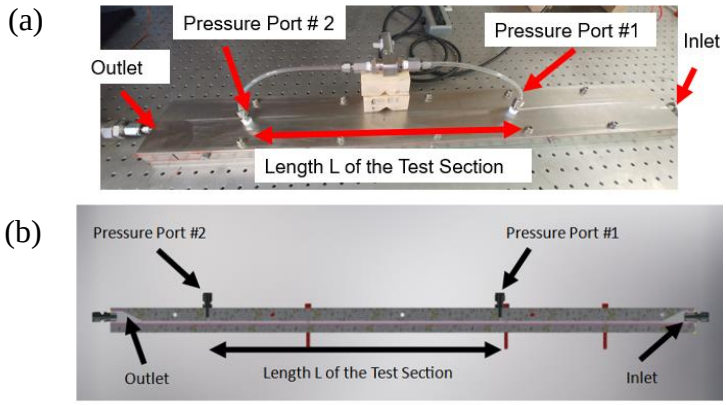

Figure 9. (a) Assembled test section. (b) Cross section view of test section.

RESULTS AND DISCUSSION

Flow Loop Validation

This section includes results to validate the accuracy of the channel flow setup. Pressure drop and volumetric flow rate data were collected for the smooth 304 stainless steel plates to compare with the literature. The hydraulic diameter, d_h, is calculated using Equation 3, where H is the height of the channel, and W is the width of the channel.

$$d_h = \frac{4*(H*W)}{2*(H+W)} \quad (3)$$

The mean velocity, U, is calculated using Equation 4, where $\dot{V}$ is the measured volumetric flow rate.

$$U = \frac{\dot{V}}{H*W} \tag{4}$$

The equation for the friction factor, f, is given in Equation 5, where L is the test section length, Δp is the pressure drop along L, and ρ is the density of the fluid.

$$f = \frac{2\Delta p d_h}{\rho U^2 L} \tag{5}$$

The equation for the Reynolds number, Re, is given in Equation 6, where ν is kinematic viscosity

$$Re = \frac{U d_h}{\nu} \tag{6}$$

After completing the tests, the friction factor with respect to the Reynolds number was plotted. Figure 10a, taken from Hartnett et al.[66], shows the experimental friction factor vs. Reynolds number from multiple experimental data available in the literature. Experimental data for the smooth plates is plotted in Figure 10b along with the Colebrook equation for turbulent flow from Figure 10a. The experimental setup was checked for repeatability by obtaining two runs for each set of plates. This process involved assembling/disassembling of the test section for additional fidelity of the experimental setup. Data was recorded after steady state was reached. The experimental data is in good agreement with the Colebrook equation.

(a)

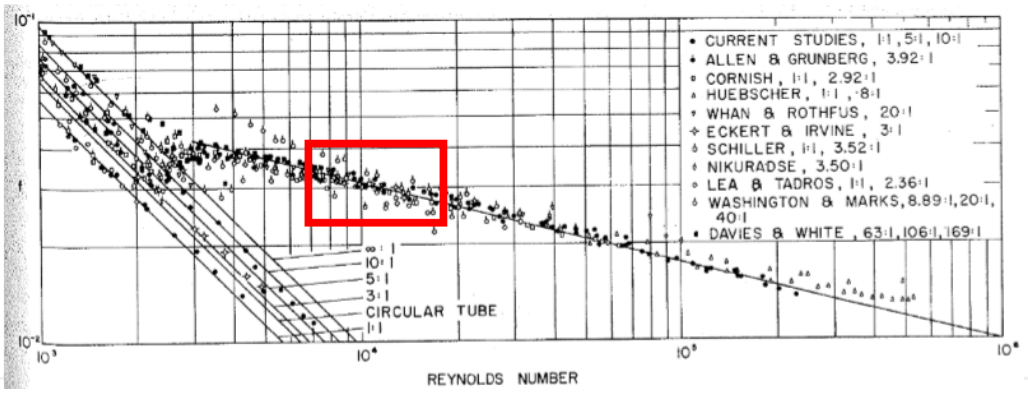

(b)

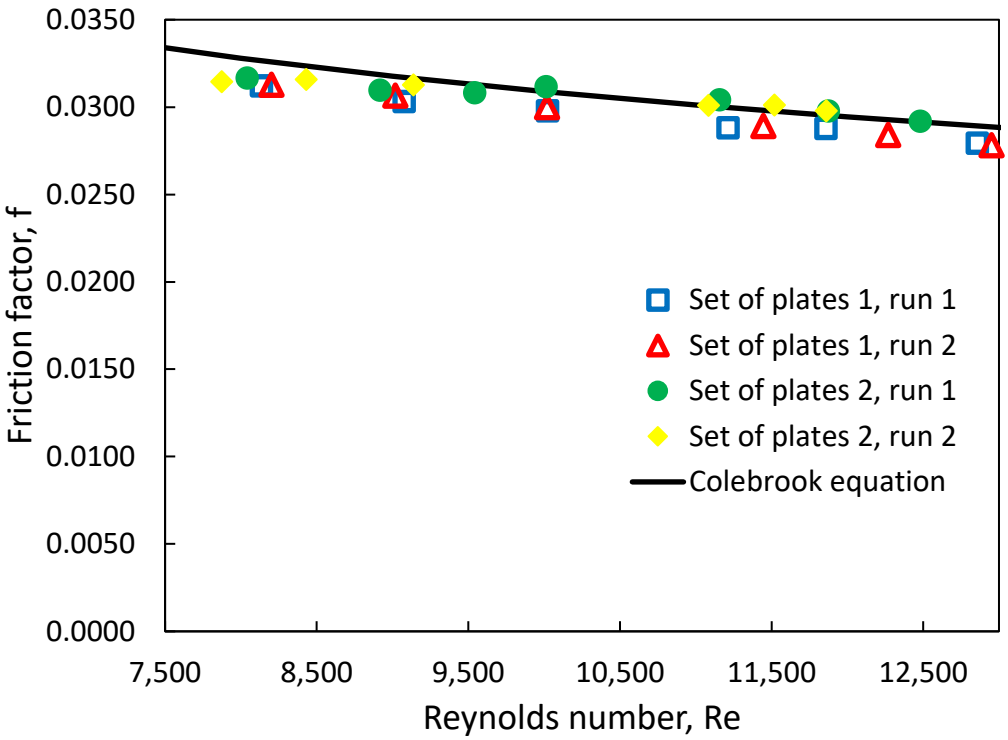

Figure 10. (a) Collection of experimental friction factor vs Reynolds number from Hartnett et al. [66]. (b) Comparison of the Colebrook equation for turbulent flow over a smooth surface and experimental data for smooth 304 stainless steel plates.

Results with Functionalized Surfaces

Drag testing for FLSP processed superhydrophilic plates

Experimental data were obtained twice (run 1 and run 2) with a set of plates (assembly 1). Following that, the test section was disassembled and assembled again (assembly 2) and two more runs were obtained. For a superhydrophilic rectangular channel with angled structures, data was collected for the pressure drop and flow rate in the same way as described above. Data for the friction factor vs Reynolds number can be seen in Figure 11a. For a superhydrophilic channel with angled structures, drag enhancement was measured with respect to smooth (unprocessed) surfaces over the same range of Reynolds numbers tested previously. The height of the processed channel is taken as the valley-to-valley distance (H_{vv}) of the microstructures on the top and bottom plates to

account for the increased wetted area due to the microstructures (see Figure 11b). There was an increase in the friction factor of 10.1% with respect to the smooth (unprocessed) surface at the highest Reynolds number tested.

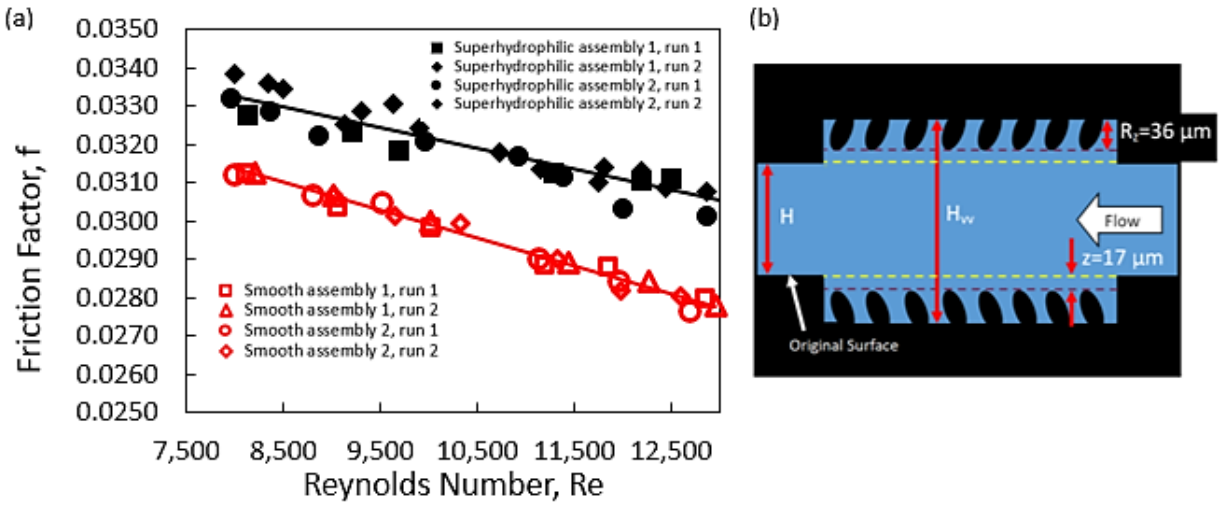

Figure 11. (a) Friction factor versus Reynolds number for the same set of 304 stainless steel plates before processing (smooth) and after processing (superhydrophilic). (b) Channel height for a fully wetted FLSP sample.

Drag testing for FLSP processed hydrophobic plates

After superhydrophilic testing was completed, the surfaces were coated with fluorinated silane using evaporative deposition that changed the plates to hydrophobic. Experimental data was collected for a hydrophobic channel with angled structures under the same flow conditions. The experimental data for friction factor vs. Reynolds number for a set of hydrophobic plates can be seen in

Figure ***12***. Drag reduction was shown for a range of Reynolds numbers that was accompanied by a plastron. When the plastron fully degraded, the surface transitioned to fully wetted, and the friction factor value shifted back towards the superhydrophilic value. The plastron degradation can be seen by the trend of the open to solid green triangles in Figure 12a. A second run that was conducted immediately after the end of run 1 exhibited friction factors similar to those measured during the superhydrophilic case (blue triangles in Figure 12a), since the plastron had fully degraded during run 1. The height of the plastron was found using a laser scanning confocal microscope. The microscope image, shown in Figure 12b, shows the top of the plastron near the peak of the microstructures. With a plastron present, the channel height is evaluated from the peak of the microstructures on the top plate to the peak of the microstructures on the bottom plate and is indicated as H_{pp}. This height is shown schematically in Figure 12c and accounts for the reduced wetted area due to the presence of the plastron. For the first four data points of run 1, the height is taken from the peak of the microstructures to account for the reduction in wetted area due to the plastron (open green triangles in Figure 12a). With a plastron present, there is a drag reduction of approximately 4% with respect to the smooth surface.

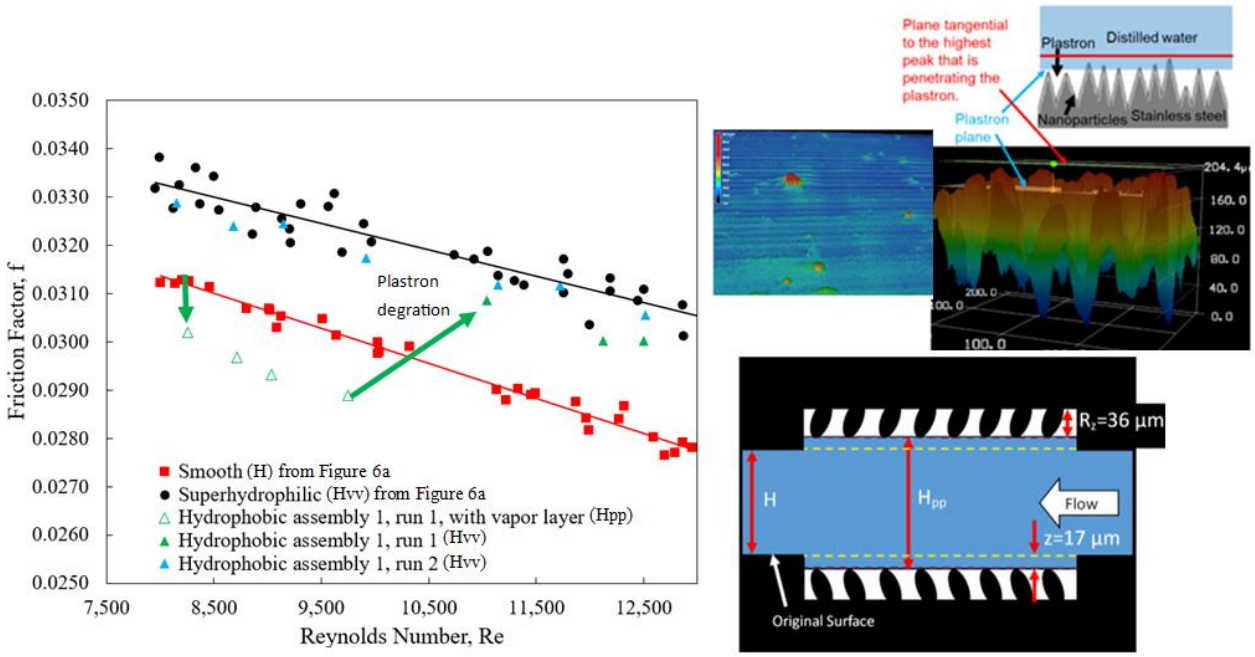

Figure 12. (a) Friction factor vs. Reynolds number for hydrophobic plates. (b) Laser scanning confocal image of the plastron height. (c) Channel height with a plastron present.

Plastron lifetime testing for FLSP processed hydrophobic plates

After testing was completed for the hydrophobic plates, the friction factor with respect to time was investigated. To investigate the friction factor with respect to time, the Reynolds number was kept constant at 9,000. Experimental data for the friction factor with respect to time is shown in Figure 13. The friction factor is evaluated at various hydraulic diameters depending on the presence of a plastron. Initially, the friction factor was evaluated with a plastron present that corresponds to Hpp. The initial friction factor value is below that for the smooth plates and shows approximately 8% reduction in friction factor. As the plastron degrades with time, the friction factor increases. During the test, air was periodically bled from the pressure ports due to an accumulation of air from the degrading plastron. At later times, when the plastron is expected to have completely degraded, the hydraulic diameter was calculated using H_{vv} and the friction factor approached a similar value to that seen with the superhydrophilic plates. The difference between the superhydrophilic channel friction factor and friction factor after the degration of the plastron is due to the small slip length caused by the low surface energy coating on the surface. In order to visualize the plastron and relate its duration to the drag behavior, a modified channel with an acrylic viewport on the sidewall was fabricated. Visualization of the plastron can be seen in Figure 14.

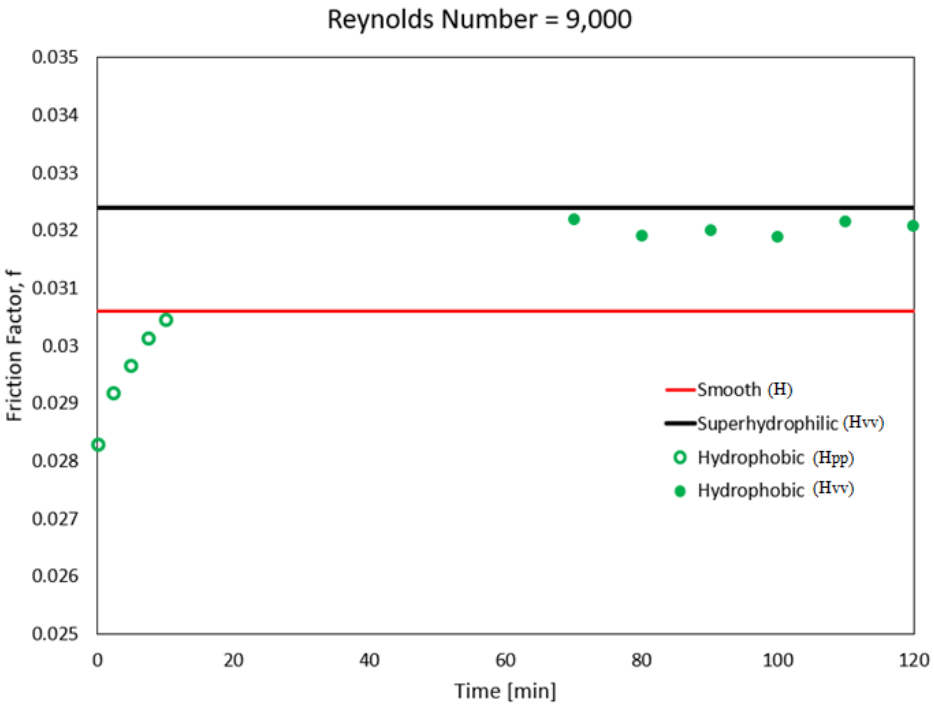

Figure 13. Friction factor versus time for constant Reynolds number.

Figure 14. Plastron visualization using the acrylic viewport.

CONCLUSIONS

304 stainless steel plates were processed via FLSP to have angled microstructures to mimic those on shark skin. For a superhydrophilic rectangular channel with angled structures, drag enhancement was measured with respect to smooth (unprocessed) surfaces over the total range of Reynolds numbers tested. There was an increase in drag of 10.1% with respect to the smooth (unprocessed) surface at the highest Reynolds number tested. For a hydrophobic rectangular channel with angled structures, drag reduction was shown for Reynolds numbers that were accompanied with a thin plastron. When the plastron fully degraded, the surface was fully wetted, and the friction factor shifted toward the superhydrophilic value.

ACKNOWLEDGMENT

This research is funded by the Office of Naval Research (ONR) Contract #FA4600-12-D-9000-17-FU909 and the NASA Nebraska Space Grant FY20 Fellowship. The research was performed in part in the Nebraska Nanoscale Facility: National Nanotechnology Coordinated Infrastructure and the Nano-Engineering Research Core Facility, which are supported by the National Science Foundation under Award ECCS: 1542182, and the Nebraska Research Initiative.

SOURCES

[1] M. Perlin and S. Ceccio, *Mitigation of Hydrodynamic Resistance: Methods to Reduce Hydrodynamic Drag* (2014).
[2] J.P. WINKLER, Reuters Press Release (2008).
[3] X. Qi and D.P. Song, Transp. Res. Part E Logist. Transp. Rev. (2012).
[4] C.L. Navier, Mémoires l'Académie Des Sci. l'Institut Fr. 389 (1823).
[5] C. Lee, C.H. Choi, and C.J. Kim, Exp. Fluids **57**, 1 (2016).
[6] K. Watanabe, Y. Udagawa, and H. Udagawa, J. Fluid Mech. **381**, 225 (1998).
[7] N.J. Shirtcliffe, G. McHale, M.I. Newton, and Y. Zhang, ACS Appl. Mater. Interfaces **1**, 1316 (2009).
[8] D. Kim and W. Hwang, J. Micromechanics Microengineering **20**, (2010).
[9] R.J. Daniello, N.E. Waterhouse, and J.P. Rothstein, Phys. Fluids **21**, 85103 (2009).
[10] K.M.T. Ahmmed, C. Patience, and A.M. Kietzig, ACS Appl. Mater. Interfaces **8**, 27411 (2016).
[11] H. Park, H. Park, and J. Kim, Phys. Fluids **25**, 110815 (2013).
[12] Y.C. Jung and B. Bhushan, J. Phys. Condens. Matter **22**, (2010).
[13] A.W. Lang and T.J. Johnson, Mech. Res. Commun. **37**, 432 (2010).
[14] J.W. Gose, K. Golovin, M. Boban, J.M. Mabry, A. Tuteja, M. Perlin, and S.L. Ceccio, J. Fluid Mech. **845**, 560 (2018).
[15] K. Watanabe, Yanuar, K. Ohkido, and H. Mizunuma, Am. Soc. Mech. Eng. Fluids Eng. Div. FED (1996).
[16] R.N. Govardhan, G.S. Srinivas, A. Asthana, and M.S. Bobji, Phys. Fluids **21**, (2009).
[17] J. Ou, B. Perot, and J.P. Rothstein, Phys. Fluids **16**, 4635 (2004).
[18] H. Park, G. Sun, and C.-J. "CJ" Kim, J. Fluid Mech. **747**, 722 (2014).
[19] C. Choi, U. Ulmanella, J. Kim, C.-M. Ho, and C.-J. Kim, Phys. Fluids **087105**, (2006).
[20] J. Ou and J.P. Rothstein, Phys. Fluids **17**, (2005).
[21] N. Kashaninejad, N.T. Nguyen, and W.K. Chan, Phys. Fluids **24**, (2012).
[22] K.B. Golovin, J.W. Gose, M. Perlin, S.L. Ceccio, and A. Tuteja, Philos. Trans. R. Soc. A **374**, (2016).
[23] J.P. Rothstein, Annu. Rev. Fluid Mech **42**, 89 (2010).
[24] P. Joseph, C. Cottin-Bizonne, J.M. Benoît, C. Ybert, C. Journet, P. Tabeling, and L. Bocquet, Phys. Rev. Lett. **97**, 1 (2006).
[25] G.D. Bixler and B. Bhushan, J. Colloid Interface Sci. **393**, 384 (2013).
[26] P. Tsai, A.M. Peters, C. Pirat, M. Wessling, R.G.H. Lammertink, and D. Lohse, Phys. Fluids **21**, 1 (2009).
[27] D. Byun, J. Kim, H.S. Ko, and H.C. Park, Phys. Fluids **20**, (2008).
[28] T.J. Kim and C. Hidrovo, Phys. Fluids **24**, (2012).
[29] D. Saranadhi, D. Chen, J.A. Kleingartner, S. Srinivasan, R.E. Cohen, and G.H. McKinley, Sci. Adv. **2**, (2016).
[30] A. Rajappan, K. Golovin, B. Tobelmann, V. Pillutla, Abhijeet, W. Choi, A. Tuteja, and G.H. Mckinley, Phys. Fluids **31**, (2019).
[31] D. Panchanathan, A. Rajappan, K.K. Varanasi, and G.H. Mckinley, ACS Appl. Mater. Interfaces **10**, 33684 (2018).
[32] H.L. Petrie, A.A. Fontaine, M.J. Moeny, and S. Deutsch, in *2006 ASME Jt. U.S.-European Fluids Eng. Summer Meet. FEDSM 2006* (2006).
[33] H.L. Petrie, T.A. Brungart, and A.A. Fontaine, Am. Soc. Mech. Eng. Fluids Eng. Div. FED (1996).

[34] S. Gogte, P. Vorobieff, R. Truesdell, A. Mammoli, F. van Swol, P. Shah, and C.J. Brinker, Phys. Fluids **17**, 1 (2005).
[35] V.M.K. K.–S. Choi, X. Yang, B. R. Clayton, E. J. Glover, M. Atlar, B. N. Semenov, K.-S. Choi, X. Yang, B.R. Clayton, E.J. Glover, M. Atlar, B.N. Semenov, and V.M. Kulik, Proc. R. Soc. **453**, 2229 (1997).
[36] E. Taghvaei, A. Moosavi, A. Nouri-Borujerdi, M.A. Daeian, and S. Vafaeinejad, Energy **125**, 1 (2017).
[37] S. Zhang, X. Ouyang, J. Li, S. Gao, S. Han, L. Liu, and H. Wei, Langmuir **31**, 587 (2015).
[38] X. Zhao, Y. Xue, H. Yang, W. Xue, F. Li, A. He, and Y. Cao, Surf. Eng. (2019).
[39] E. Aljallis, M.A. Sarshar, R. Datla, V. Sikka, A. Jones, and C.H. Choi, Phys. Fluids **25**, (2013).
[40] A.A. Fontaine, S. Deutsch, T.A. Brungart, H.L. Petrie, and M. Fenstermacker, Exp. Fluids (1999).
[41] S. Deutsch, A.A. Fontaine, M.J. Moeny, and H.L. Petrie, J. Fluid Mech. (2006).
[42] H.L. Petrie, S. Deutsch, T.A. Brungart, and A.A. Fontaine, Exp. Fluids **35**, 8 (2003).
[43] B.R. Elbing, E.S. Winkel, K.A. Lay, S.L. Ceccio, D.R. Dowling, and M. Perlin, J. Fluid Mech. **612**, 201 (2008).
[44] Y. Tuo, H. Zhang, W. Rong, S. Jiang, W. Chen, and X. Liu, Langmuir (2019).
[45] C. Byon, Y. Nam, S.J. Kim, and Y.S. Ju, in *J. Appl. Phys.* (2010), pp. 9–12.
[46] B. Bhushan and Y.C. Jung, Prog. Mater. Sci. **56**, 1 (2011).
[47] K.M. Tanvir Ahmmed and A.-M. Kietzig, Soft Matter **12**, 4912 (2016).
[48] P.S. Virk, AIChE J. **21**, 625 (1975).
[49] P.S. Virk, J. Fluid Mech. **45**, 417 (1971).
[50] J.S. Park and M.D. Graham, J. Fluid Mech. **782**, 430 (2015).
[51] S.-Q. Yang, J. Fluids Eng. **131**, 051301 (2009).
[52] P.K. Ptasinski, F.T.M. Nieuwstadt, B.H.A.A. Van Den Brule, and M.A. Hulsen, Flow, Turbul. Combust. **66**, 159 (2001).
[53] R.D. Whalley, J.S. Park, A. Kushwaha, D.J.C. Dennis, M.D. Graham, and R.J. Poole, Phys. Rev. Fluids **2**, 034602 (2017).
[54] C.F. Li, R. Sureshkumar, and B. Khomami, Phys. Rev. E **92**, (2015).
[55] B.A. Toms, Proc. 1st Int. Congr. Rheol. **2**, 135 (1948).
[56] B.R. Solomon, K.S. Khalil, and K.K. Varanasi, Langmuir **30**, 10970 (2014).
[57] W. Chen, A.Y. Fadeev, M.C. Hsieh, D. Öner, J. Youngblood, and T.J. McCarthy, Langmuir **15**, 3395 (1999).
[58] A.B.D. Cassie and S. Baxter, Trans. Faraday Soc. **40**, 546 (1944).
[59] P.-G. de Gennes, F. Brochard-Wyart, and D. Quéré, *Capillarity and Wetting Phenomena* (2004).
[60] D. Quéré, Phys. A Stat. Mech. Its Appl. **313**, 32 (2002).
[61] H.J. Ensikat, P. Ditsche-Kuru, C. Neinhuis, and W. Barthlott, Beilstein J. Nanotechnol. (2011).
[62] P. Bizi-Bandoki, S. Benayoun, S. Valette, B. Beaugiraud, and E. Audouard, Appl. Surf. Sci. **257**, 5213 (2011).
[63] C.A. Zuhlke, T.P. Anderson, and D.R. Alexander, Appl. Phys. Lett. **103**, (2013).
[64] A. Hassebrook, M.J. Lucis, J.E. Shield, C.A. Zuhlke, T.P. Anderson, D.R. Alexander, G. Gogo, and S. Ndao, in *Proc. ASME 2015 13th Int. Conf. Nanochannels, Microchannels, Minichannels Collocated with ASME 2015 Int. Tech. Conf. Exhib. Packag. Integr. Electron. Photonic Microsyst.* (2015), pp. 1–7.
[65] C.A. Zuhlke, T.P. Anderson, P. Li, M.J. Lucis, N. Roth, J.E. Shield, B. Terry, and D.R. Alexander, in *Laser-Based Micro-Nanoprocessing IX* (2015).
[66] J.P. Hartnett, J.C.Y. Koh, and S.T. McComas, J. Heat Transfer **84**, 82 (1962).